Breast Cancer: Targets and Therapy

Dovepress

open access to scientific and medical research

Open Access Full Text Article

ORIGINAL RESEARCH

An Magnetic-Targeting Nano-Diagnosis and Treatment Platform for TNBC

Mengqi Zhang[1,*], Shengxian Bao[2,*], Guanhua Qiu[2,*], Jingchen Liang[2], Qin Wang[2], Xiaoqi Zhu[2], Guchun Qin[1], Junjie Liu[2], Chang Zhao[1]

[1]Department of Interventional Therapy, Affiliated Tumor Hospital of Guangxi Medical University, Nanning, People's Republic of China; [2]Department of Ultrasound and Department of Radiology, Affiliated Tumor Hospital of Guangxi Medical University, Nanning, People's Republic of China

*These authors contributed equally to this work

Correspondence: Junjie Liu; Chang Zhao, Email liujunjie197806@163.com; 710519137@qq.com

Purpose: In this experiment, we constructed a magnetic targeting nano-diagnosis and treatment platform of doxorubicin (DOX) combined with iron nanoparticles, and explored their application value and mechanism in the treatment of Triple Negative Breast Cancer (TNBC), as well as its new diagnosis and treatment mode in Magnetic Resonance Imaging (MRI).

Patients and Methods: Hollow mesoporous nanoparticles (HFON) were synthesized by solvothermal method, and loaded the drug DOX (DOX@HFON) to treat TNBC. The experiments in vivo and in vitro were carried out according to the characteristics of the materials. In vitro experiments, the killing effect of the drug on cells was verified by cell viability CCK8, ROS generation level, LPO evaluation and flow cytometry; the MRI effect and targeted anti-tumor therapy effect were studied by in vivo experiments; then the tumor tissue sections were detected by Ki-67, CD31, ROS, LPO and TUNEL immunofluorescence detection; H&E staining and blood biochemical tests were used to evaluate the biosafety of the materials.

Results: Through a series of characterization tests, it is confirmed that the nano-materials prepared in this experiment have positive drug loading properties. MDA-MB-231 cells had great phagocytic ability to DOX@HFON under Confocal Laser Scanning Microscope (CLSM). Experiments in vitro confirmed that DOX and Fe were released and concentrated in cells, and a large number of ROS production and induction of LPO were detected by DCFH-DA and C11-BODIPY probes in cells. Apoptosis experiments further confirmed that DOX@HFON induced apoptosis, autophagy and ferroptosis. In the vivo experiment, the anti-tumor therapy effect of MAGNET@DOX@HFON group was the most significant, and in MRI also proved that the drug had great tendency and imaging ability in tumor tissue.

Conclusion: The new magnetic targeting nano-diagnosis and treatment platform prepared in this experiment is expected to become a new treatment model for TNBC.

Keywords: nanoparticles, DOX, Fenton, ROS

Introduction

In recent years, major breakthroughs have been made in cancer treatment research, but the harm caused by cancer still seriously affects human health. Breast Cancer is the most common cancer in women, accounting for approximately 12–14% of all cancer cases worldwide.[1] Among them, TNBC is a special type of breast cancer that is widely known to occur in premenopausal women. It is called TNBC because its Estrogen Receptors, Progesterone Receptors and Human Epidermal Growth Factor Receptor 2 are all negative, The incidence of breast cancer accounts for 15–20% of all subtypes of breast cancer,[2] and the recurrence rate within three years after diagnosis is extremely high. The overall prognosis of TNBC is poor due to the lack of typical molecular targets. For patients, chemotherapy is the only option.[3]

As a broad-spectrum antitumor drug, DOX can actively insert into cellular DNA and disrupt topoisomerase II-mediated DNA repair,[4,5] and is currently widely used in breast cancer, osteosarcoma, and lymphoma and other clinical drugs.[6–10] Studies have shown that DOX can also activate Nicotinamide Adenine Dinucleotide Phosphate Oxidase

Received: 27 August 2022
Accepted: 12 January 2023
Published: 3 February 2023

(NADPH Oxidase, NOX) to generate H_2O_2.[11,12] Although the effect of DOX in the tumors treatment is considerable, it often causes serious adverse reactions and drug resistance.[13] Therefore, it is a challenging goal to develop new cancer treatment options that can not only effectively fight cancer but also reduce toxic and side effects.

The emergence of nanotechnology has attracted great attention of researchers. Nanoparticles are considered to be an important way to selectively increase drug accumulation in tumor cells so as to reduce related side effects.[14,15] Liposome, as a microbubble formed in a lipid-like bilayer structure, can effectively protect drugs from hydrolysis or oxidative degradation by its unique bilayer membrane, thus minimizing toxicity.[16] Liposome drug delivery system has been widely studied to improve the therapeutic effect of chemotherapy. Liposome doxorubicin has entered Phase II and III clinical trials due to its great drug loading performance and stability, as well as low cytotoxicity. FDA approved clinical use in MBC.[17,18] However, there are still some problems, such as low drug loading, poor non-specificity and lack of controlled release, which seriously affect the clinical application of liposome doxorubicin.[19,20] It is worth noting that the application of iron-based catalytic Fenton reaction in tumor therapy also in full swing.[21,22] The Fenton reaction is catalyzed by Fe^{2+} to consume H_2O_2 to generate strong oxidizing •OH,[23–25] and induce a large number of ROS production, and excessive ROS can disrupt the redox homeostasis, resulting in irreversible production of lipids, mitochondria and nuclear DNA, further lead to apoptosis, autophagy and ferroptosis, so as to achieve the purpose of tumor treatment.[26,27] Studies have found that the unique cell proliferation, metabolic activity, DNA alternation and mitochondrial dysfunction of tumor cells promote the overproduction of H_2O_2, which also provides a favorable environment for the occurrence of the Fenton reaction.[28] Therefore, the reaction of converting endogenous H_2O_2 into highly toxic •OH can be applied to tumor therapy by introducing nano-iron catalysts into tumor cells/tissues. Xu et al prepared Fe^{2+} based Metal Organic Framework (MOF) nanoparticles to release Fe^{2+} in response to pH degradation in acidic Tumor-Microenvironment (TME), enhancing the Fenton reaction and the ability to generate ROS, thereby inducing tumor cell apoptosis.[29–31] It can be seen that the Fenton reaction induces excessive production of ROS, and then disrupts the redox homeostasis in tumor cells to promote the cascade reaction of apoptosis, which has certain prospects in tumor therapy.[23,32] It is worth noting that the content of iron in the human body is very low, and most of this iron is combined with some specific proteins to maintain the basic homeostasis of the human body. Therefore, if the iron nanoparticles can be targeted and transported into tumor cells, it can effectively promote the occurrence and development of the Fenton reaction, so as to achieve the purpose of treating tumors.

In this study, we prepared a hollow mesoporous ferric oxide nanoparticle HFON based on a solvothermal method, combined with the drug DOX (DOX@HFON), and simultaneously targeted and transported HFON to tumors by introducing an exogenous magnetic field Intracellular (MAGNET@DOX@HFON), further enhancing its ability to kill tumor cells. Not only that, we also use HFON unique imaging technology to verify the distribution of the drug in the body and its role in disease-specific diagnosis, and conduct a new tumor synergistic treatment model for TNBC (Figure 1).

Materials and Methods

Materials

$FeCl_3$ (10025–77-1), Ethylene Glycol (E103319), Ammonium acetate (10534–59-5), Doxorubicin (23214–92-8) was purchased from Aladdin (Shanghai, China). Ethanol anhydrous (64–17-5) was purchased from Macklin (Shanghai, China). High temperature drying oven (XMTD8222) was purchased from Jinghong (Shanghai, China). FBS and penicillin/streptomycin were purchased from BI (CA, USA). The DMEM cell culture media were purchased from Solarbio (Beijing, China).

Preparation of Nanoparticles

Prepare an ethylene glycol solution with a solute content of 19.28 mg/mL $FeCl_3$, add the corresponding content of CH_3COONH_4 to neutralize free chloride ions, shake and mix with an ultrasonic device, continue hydrothermal reaction in a drying box for 16.5 h, and reduce to routine temperature. Collection using magnetic properties. After washing with anhydrous ethanol four times, the above operation was repeated with deionized water, and stored in a refrigerator at

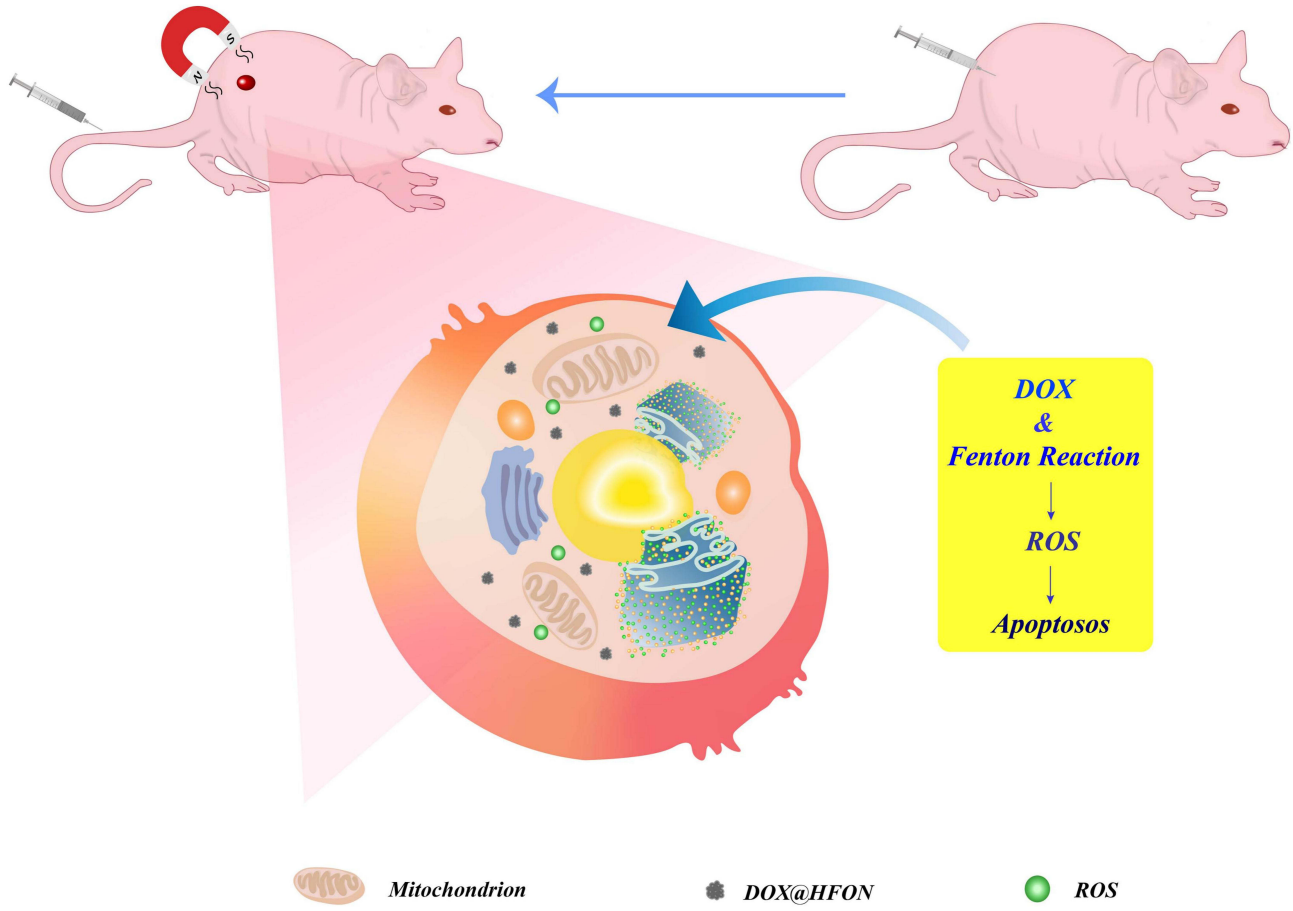

Figure 1 Schematic illustration of the process of DOX@HFON for cancer therapy.

4°C for later use, and finally HFON was obtained.

Subsequently, 1 mL (10 mg of solute) of HFON and 40 μL (1 mg of solute) of DOX were placed on a shaker and incubated at 100 rpm for 2 h, and the free DOX was filtered out by magnetic properties, and finally suspended in deionized water and placed at 4°C store in the refrigerator for later use, and obtain the nanoparticles DOX@HFON.

Characterization

The DOX@HFON was loaded into a centrifugal tube and dried into powder in a freeze dryer, then the morphology was analyzed by SEM (Ultra Plus, Zeiss, Germany) and BET (ASAP2460, Mike, USA) to analyze the specific surface area of nanoparticles, the appropriate amount of DOX@HFON solution was analyzed by TEM (Tecnai G2 USA) for energy spectrum and element analysis; the particle size and potential of HFON and DOX@HFON were detected by DLS (Zeta Plus, Brookhaven, USA); The chemical elements and distribution of DOX@HFON were analyzed by EDS (GENESIS XM, EDAX, USA) and XPS (ESCALAB 250Xi, Thermo Fisher, USA); the absorbance of DOX@HFON at different concentrations was calculated by detecting the UV-Vis of DOX@HFON, and further draw a standard curve; the characteristic signals of •OH was acquired via ESR spectrometer (A300-10/12, Bruker, German); description of crystalline structure of HFON by XRD (Brucker D8 Advance, German); DOX@HFON was diluted with quantitative standards of different Fe concentrations, and then scanned by GE 3.0T MRI. Scanning conditions: TR: 2000ms, TE: 76.74, FOV: 19×15cm, Matrix: 320× 256; and the T2 relaxation time of each sample was measured, and the image was drawn according to the inverse T2 relaxation time and the corresponding iron concentration; VSM (PPMS-9, Quantum Design, USA) was used to evaluate the superparamagnetic properties of DOX@HFON; at routine temperature the DOX@HFON solution was placed on a shaker for continuous shaking, and the absorbance of the supernatant was measured at different

time points, and finally the in vitro release curve of DOX drawn; Fe release were performed using an iron assay kit (Abcam, USA). At routine temperature the HFON was inoculated with Fe probe, and measurement of total iron (Fe^{2+}, Fe^{3+}) were performed following the manufacturer's instructions; DOX@HFON was dissolved in PBS and 10% FBS at routine temperature, then placed on a shaker for continuous shaking, and the supernatant was determined at different time points to detect the stability of DOX@HFON in different solutions.

Cell Line and Culture Condition

The cells used in this experiment were Human Breast Cancer Cells MDA-MB-231 and Human Umbilical Vein Endothelial Cells (HUVEC), which were purchased from Guangzhou Yeshan Biotechnology Co. Ltd. HUVEC and MDA-MB-231 cells were grown in DMEM medium supplemented with 10% FBS and 1% penicillin-streptomycin solution. All cell were grown at 37 °C in the presence of 5% CO_2.

CCK8 Assays

The toxic effect of DOX@HFON on MDA-MB-231 cells was detected by Cell Counting Kit-8 (CCK8) (35002, DOJINDO, Japan). MDA-MB-231 cells grown in logarithmic phase were seeded in a 96-well plate at a density of 5000 cells per well, and incubated overnight in a 5% CO_2 incubator. The next day, cells were replaced with different concentrations of DOX@HFON (five duplicate wells were set), and incubated again in the incubator for 24 h. Then, add 10 μL of CCK-8 reagent to each well and incubate for 4 h in the dark in a 5% CO_2 incubator. Finally, the absorbance at 450 nm of each well was detected under a microplate reader (multiscan MK3, Thermo Fisher, USA), and the data was analyzed by GraphPad.

Cellular Uptake

MDA-MB-231 cells pretreated with DOX@HFON were collected at low temperature, and 2.5% glutaraldehyde fixative was added overnight at 4 °C after low-speed centrifugation. The next day, the samples were washed and put into different concentrations of ethanol and acetone in turn for dehydration, so that the cells could be fully embedded. Ultrathin sectioning was then performed under a microscope with a thickness of 60 nm. The uranyl acetate dye was dropped on wax paper, and the sections were immersed in the dye solution for 15 min, and then washed with water. After drying, they were observed and photographed using a TEM (Tecnai G2 F30, FEI).

In addition, in order to further prove the drug targeting and the phagocytosis level of the drug, MDA-MB-231 cells were inoculated into laser confocal special petri dishes and incubated overnight in hypoxia incubator, and DOX@HFON was added to the petri dishes at different time points the next day. Then, the supernatant was absorbed and washed with PBS for 3 times. The nucleus was stained with 80 μL Hoechst 33,342 for 15 min, then washed again for 3 times. Finally, the cells were observed by CLSM (Leica SP8, Germany) imaging.

Detection of Iron Concentration

In this experiment, Prussian blue staining kit (DJ0001, Leigen, China) was used to detect the ability of cells to uptake Fe. Cells grown in logarithmic phase were seeded in 6-well plates at a density of 1×10^5 cells per well, and the experiments were divided into Control group, HFON group, and DOX@HFON group, and incubated overnight in a 5% CO_2 incubator; respectively, in the supernatant add 50 μg/mL HFON and DOX@HFON to the solution for 24 h. Cells were washed with PBS and fixed with 4% paraformaldehyde for 20 min. Treat with Perls stain mixture for 10 min, wash off excess mixture, add nuclear fast red staining solution to lightly stain cell nuclei, rinse for 5 s, mount with neutral gum and observe under microscope.

Detection of ROS Generation

In vitro ROS generation assay was performed using the fluorescent probe DCFH-DA (S0033-1, Beyotime, China). Cells grown in logarithmic phase were seeded in 6-well plates at a density of 1×10^5 cells per well. The experiments were divided into Control group, HFON group, and DOX@HFON group, and incubated overnight in a 5% CO_2 incubator; 50 μg/mL HFON and DOX@HFON were added to the cells and incubated for 2 h, DCFH-DA diluted 1:1000 was added to

each well, incubated in the dark for 20 min, washed 3 times with PBS, and photographed with an inverted fluorescence microscope. The excitation wavelength was 488 nm, and the emission wavelength is 525 nm.

In vitro LPO Evaluation

The above experiments confirmed the level of drug uptake by cells and the production of ROS, and then we observed the mechanism of drug action by LPO experiments in vitro. The cells growing in logarithmic phase were inoculated in 6-well plate with the density of 1×10^5 cells per well. The experimental groups were divided into Control group, HFON group and DOX@HFON group, which were incubated overnight in 5% CO_2 incubator. 50 μg/mL HFON and DOX@HFON were added to each hole to incubate overnight, and then 1:1000 diluted C11-BODIPY (D3861, Thermo, Fisher, USA) was added to each well for 30 min. Washing by PBS for 3 times without light. The photo was taken with an inverted fluorescence microscope with excitation wavelength of 581 nm and emission wavelength of 591 nm.

Cell Apoptosis Assay

The cells grown in logarithmic phase were seeded in a 6-well plate at a density of 1×10^5 cells per well, and the experiments were divided into Control group, HFON group, and DOX@HFON group, and incubated overnight in a 5% CO_2 incubator; Add 50 ug/mL HFON and DOX@HFON to incubate for 24 h; digest with 0.25% trypsin without EDTA, collect and wash cells, resuspend in buffer, add 1.25 μL Annexin V-FITC at 4°C. Cells were fluorescently labeled with 10 μL Propidium Iodide, and finally analyzed by flow cytometry (CALIBUR, BD, USA), and the data was processed by FlowJo software.

Angiogenesis Assay

HUVEC cells grown in logarithmic phase were seeded in 6-well plates at a density of 1×10^5 cells per well. The experiments were divided into Control group, HFON group, and DOX@HFON group, and incubated overnight in a 5% CO_2 incubator. After freezing and thawing, Matrigel (354,230, BD, USA) was added to a 48-well plate at 200 μL per well, and placed in an incubator to incubate until coagulation; when the cells grew to 80–90%, digest the cells and use 2×10^4 cells per well. The cells were seeded in Matrigel 48-well plates, and 50 μg/mL HFON and DOX@HFON were added to each well for incubation for 24 h; the formation of blood vessels was observed after 6 h. Finally, the 5×10^4 growing in logarithmic phase was inoculated in 96-well plate, and the above steps were repeated. The inhibitory effect of the drug on angiogenesis was analyzed by detecting its OD value.

Anticancer Therapy in vivo

All animal experiments were approved by the Institutional Animal Care and Use Committee of the Cancer Hospital Affiliated to Guangxi Medical University, Approval number: LW2022144. Animal ethics review follows the Guiding Opinions on the Treatment of Laboratory Animals issued by the Ministry of Science and Technology of the People's Republic of China and the Laboratory Animal-Guideline for Ethical Review of Animal Welfare issued by the National Standard GB/T35892-2018 of the People's Republic of China.

Based on the superparamagnetic characteristics of HFON, we use strong magnetic sheets to fix the tumor to target and attract the drugs to gather at the tumor site to enhance the curative effect and reduce the toxic and side effects of chemotherapeutic drugs. All 4-week-old nude mice were randomly divided into 4 groups (n=5), and received different treatments: Control group, HFON group, DOX@HFON group, MAGNET@DOX@HFON group. MDA-MB-231 cells (5×10^6 cells in 100 μL of PBS per mice) were subcutaneously inoculated on the back of the mice; when the tumor grew to 4–5 mm, 100 μL drug treatment was started through the tail vein, among which MAGNET@DOX@HFON after the administration of the group, a magnetic block was fixed at the tumor site. Each treatment interval was 2 days, a total of 3 times; the body weight and tumor size of the mice were measured once every 3 days, and the volume was calculated, such as the formula:

$$\text{volume} = \frac{\text{length} * \text{width} * \text{width}}{2} \left(\text{mm}^3\right)$$

On the 18th day of treatment, mice were sacrificed by cervical dislocation and tumor tissues and major internal organs (heart, liver, spleen, lung and kidney) were collected for immunofluorescence, TUNEL and H&E staining analysis.

In vivo MR Imaging

4-week-old nude mice were randomly divided into two groups (n=3): DOX@HFON group and MAGNET@DOX@HFON group; MDA-MB-231 cells (5×10^6 cells in 100 μL of PBS per mice were subcutaneously inoculated on the back of the mice; when the tumor grows to be suitable for imaging, after administration through the tail vein, the magnetic block was fixed at the tumor of the mice in the MAGNET@DOX@HFON group, and GE3.0T MRI was used for MRI T2-weighted imaging studies at different time points (0 h, 2 h, 4 h, 6 h after injection).

Iron Enrichment in Mouse Tumor

The transplanted tumor was fixed in 4% paraformaldehyde fixative solution for 24 h, then immersed in alcohol from low to high concentration for dehydration, and then the tissue was placed in xylene for transparency, and then placed in melted paraffin for embedding after cooling and solidification, it was fixed on a microtome, cut into 5-μm thick sections, and pasted on a glass slide to successfully prepare paraffin sections. Next, the paraffin sections of mice tumors were deparaffinized according to conventional methods, and stained with Prussian blue after hydration. Images were observed and photographed using a biofluorescence inverted microscope (BX63, Olympus).

Immunofluorescence Staining

Collect mice tumors to prepare paraffin sections (deparaffinized and hydrated according to the above method), Ki-67 Polyclonal Antibody (PA5-19,462, Thermo Fisher USA) was used for Ki-67 staining, dilution ratio: 1:1000; DCFH-DA (S0033-1, Beyotime, China) was used for ROS staining, dilution ratio: 1:1000; C11-BODIPY (D3861, Thermo, Fisher, USA) was used for LPO staining, dilution ratio: 1:1000; and Rabbit was used for CD31 staining anti-CD31 (ab218582, ABCAM, China), dilution ratio: 1:100, DAPI was used to stain nuclei. Finally, the immunohistochemical staining images were captured and photographed with a biofluorescence microscope.

The pretreatment of tumor paraffin sections was the same as above. After deparaffinization, 20 μg/mL Proteinase K was added dropwise to the sections to prepare Proteinase K working solution, and then incubated in a 37°C incubator for 20 min. The sections were washed 3 times with PBS, and then 50 ul of the prepared TUNEL detection solution was added dropwise evenly. After incubation in the dark for 1 h, the PBS was taken out and washed three times. After DAPI staining and mounting, the images were observed and photographed under a fluorescence microscope.

Biological Safety Evaluation

Twelve tumor-bearing mice were randomly divided into 4 groups (Control group, HFON group, DOX@HFON group, MAGNET@DOX@HFON group), 3 mice in each group, and were administered with tail vein injection every 2 days. The dose was the same as that in vivo anti-tumor experiment, and then the main organs (heart, liver, spleen, lung and kidney) of the mice were collected at different time points for H&E staining, and serum samples were collected for biochemical analysis (TBIL, DBIL, AST, ALT, CREA, UREA, UA).

Statistics

Each experiment was repeated at least 3 times. The numerical results were expressed as mean ± SD, statistical significance between the groups was compared by Student's *t*-test (two-sided) or one-way analysis of variance (ANOVA). All statistics are conducted with SPSS 24.0 (IBM Corporation, USA). The pictures were drawn using GraphPad Prism 8.0 (San Diego, CA). (n.s: not significant, *$P < 0.05$, ** $P < 0.01$, and *** $P < 0.001$).

Results

Preparation and Characterization of HFON Before and After DOX Conjugation

In this experiment, nanomaterials were synthesized by solvothermal method. In TEM, BET and SEM images (Figures 2A and S1A-C), it can be seen that HFON is a hollow spherical particle with uniform size, and there is no obvious change in particle size before and after freeze drying; the particle size and potential changes of HFON before and after drug loading

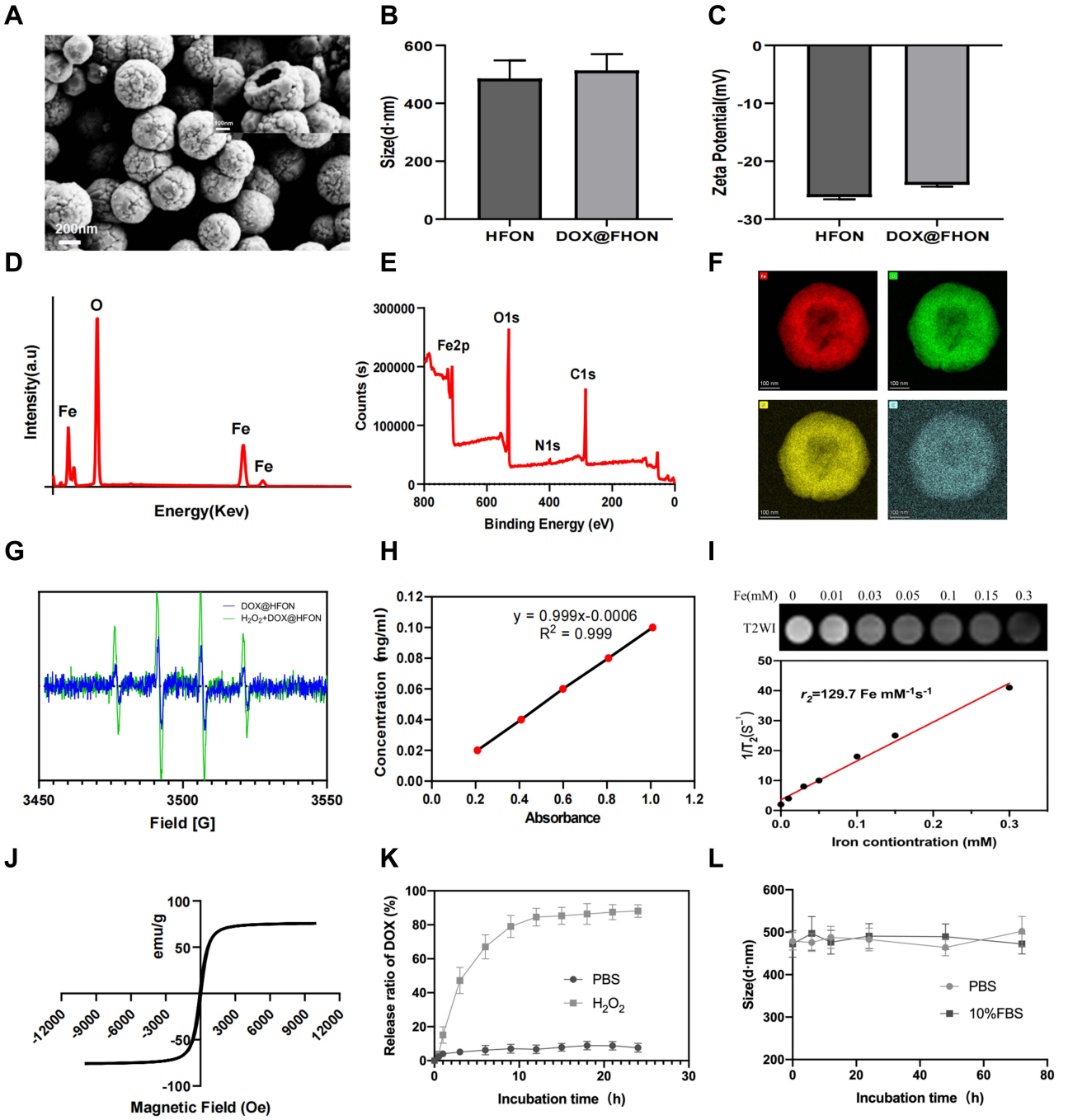

Figure 2 Characterization and detection of HFON and DOX@HFON: (**A**) SEM images of HFON and the inserted picture is HFON cross section SEM image; (**B** and **C**) DLS and Zeta detection results of HFON and HFON loaded with DOX; (**D**) EDS spectrum and quantitative analysis results of DOX@HFON; (**E**) XPS spectrum of DOX@HFON; (**F**) Mapping result of DOX@HFON, including Fe, O, N and C element; (**G**) ESR detection of HFON and DOX@HFON: ability to generate • OH; (**H**) Standard curve of DOX@HFON; (**I**) T2 relaxation rate of DOX@HFON, and T2-weighted images under different iron concentrations (mM); (**J**) The hysteresis curve of DOX@HFON. (**K**) DOX@HFON release curve in vitro; (**L**) Stability detection of DOX@HFON in PBS and 10% FBS.

were detected by DLS (Figure 2B and C). The particle size of HFON was 486 ± 63 nm and the Zeta potential was −26.2 ± 0.4 mV ($P >$ ns), while the particle size and Zeta potential of DOX@HFON only changed slightly after loading the drug, which were 513 ± 57 nm and −24.0 ± 0.4 mV, respectively, confirming that the successful loading of the drug has not affected the properties of the carrier itself; EDS, XPS and MAPPING (Figure 2D–F) confirmed that the four elements Fe, O, C and N are uniformly distributed in DOX@HFON and successful loading of drugs, among which Fe and O have the highest atomic content, its percentage is very similar to Fe_3O_4; The crystalline structure of HFON was confirmed by X-Ray Diffraction (XRD) pattern (Figure S1D); 5-dimethyl-1-pyrrolidine N-oxide (DMPO) was used to measure the ability of DOX@HFON to produce •OH in vitro. It is observed in Figure 2G that DOX@HFON showed strong characteristic •OH signal in H_2O_2 environment. Therefore, we think that DOX@HFON can effectively catalyze H_2O_2 in tumor to produce cytotoxic •OH; The characteristic absorption peak of DOX@HFON detected by UV-Vis is about 480 nm, and the standard curve is drawn according to the absorbance of different concentrations of DOX@HFON, as shown in Figure 2H. The entrapment efficiency and drug loading rate are 60.04% and 6.00%, respectively; in MRI T2-weighted imaging (Figure 2I), it could be found that with the increase of Fe concentration, the T2 signal intensity gradually weakened, and it was calculated that r^2=129.7 $FemM^{-1}s^{-1}$, it reflects the perfect MRI imaging performance of DOX@HFON; at the same time, the magnetic induction intensity of DOX@HFON increases with the increase of the applied magnetic field intensity, and the magnetic induction intensity begins to saturate when the applied magnetic field intensity reaches about 2000 (Oe) (Figure 2J); As shown in Figure 2K, L and S1E, the cumulative release of DOX and Fe in H_2O_2 both showed a gradually increasing trend, and the release rate could reach 88.56%, 62.74% by 24 h, at the same time, the particle size of DOX@HFON in PBS and 10% FBS solutions did not change significantly. The stability of DOX@HFON, good drug delivery performance and MRI imaging effect were confirmed by characterization test.

Cellular Uptake Under TEM

The ingestion and phagocytosis of nanoparticles by tumor cells is an important prerequisite for the anti-tumor effect. In this experiment, TEM and CLSM were used to detect the phagocytosis of DOX@HFON by MDA-MB-231. As shown in Figure 3A, deep-stained metal particles can be seen in the cells of the final group, indicating that MDA-MB-231 cells can engulf DOX@HFON by endocytosis. DOX@HFON was delivered to the cytoplasm to play a role. At the same time, the changes in the cell structure after the drug treatment in each group were observed under TEM. From Figure 3B, we found that the cells in the Control group had complete morphological structure, loose chromatin, complete intracellular mitochondrial structure, and clear outline of mitochondrial cristae. In the HFON group, there were multiple microvesicles and autophagolysosomes, and mitochondria were vacuolated, indicating that Fe can induce autophagy induced by changes in the mitochondrial structure of tumor cells. The cells in the DOX@HFON group showed budding phenomenon, the nucleus was pyknotic and irregular in shape, the intracellular mitochondria appeared vacuolated and the mitochondrial cristae partially disappeared, and autophagosomes with multi-layer membrane structure were seen. This further confirmed the mechanism by which DOX@HFON could induce autophagy and apoptosis in tumor cells.

At the same time, through the observation of drug uptake by cells under CLSM (Figure 3C), it was found that only uniform blue stained nuclei could be seen at 0 h after the addition of the drug. With the increase of time, the gradually enhanced red fluorescence (DOX) surrounded the nucleus in the DOX@HFON group. The drug had entered the cell at 2 h, and the red fluorescence was the strongest at 6 h, indicating that DOX@HFON could be efficiently swallowed by MDA-MB-231 cells. It has laid a good foundation for the follow-up tumor treatment.

In vitro Iron Distribution

The accumulation of high concentrations of intracellular iron ions is the key to the occurrence of Fenton reaction. Prussian blue staining is a qualitative and intuitive method to observe the distribution of iron ions in cells. It can be seen from Figure 4A that the blue-stained nanomaterial in MDA-MB-231 cells indicate that HFON and DOX@HFON are largely taken up by cells through endocytosis, resulting in an increase in the concentration of intracellular Fe. It can be seen that there is a large amount of Fe in the cells after treatment with HFON and DOX@HFON, which provides favorable conditions for the Fenton reaction to generate highly toxic ROS and further complete tumor treatment.

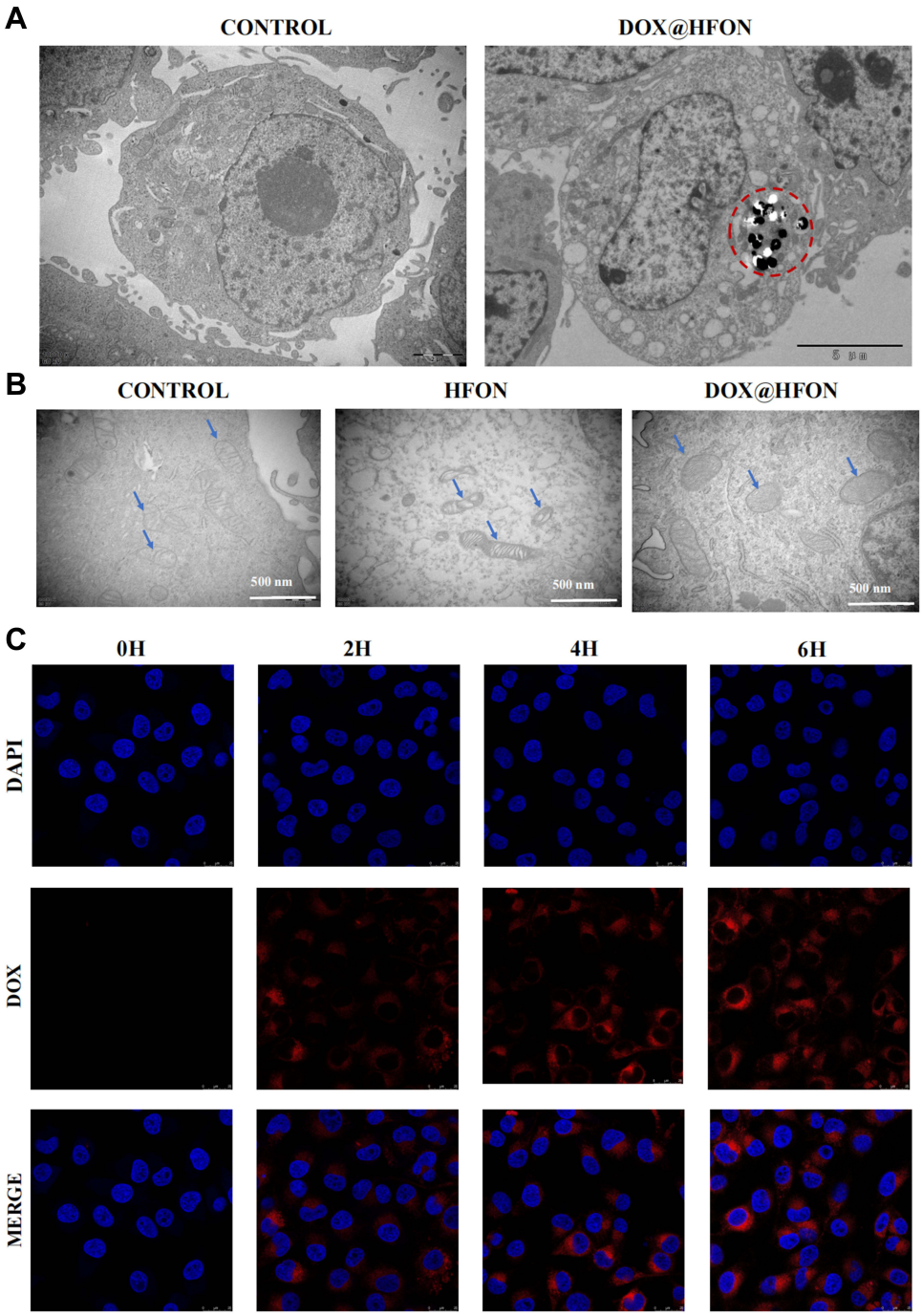

Figure 3 (**A**) Phagocytosis of DOX by MDA-MB-231 cells under TEM; (**B**) Under TEM, the changes of cell structure after drug action; (**C**) Phagocytosis of drug by cells under confocal microscope.

ROS Generation Assay and LPO Evaluation

HFON and DOX@HFON generate a large amount of ROS in cells through the Fenton reaction, which induces tumor cell apoptosis. Since ROS is the main effector product of the Fenton reaction, we examined the generation of intracellular ROS. As shown in Figures 4B and S2, the fluorescence intensity of cells treated with HFON was significantly stronger than that of the Control group (***P<0.001), which verifies that the lipid peroxidation of cells through the Fenton reaction disrupts the redox homeostasis and promotes the production of ROS. It is worth noting that compared with the HFON group and the Control group, the green fluorescence of the DOX@HFON group was the strongest, and the results

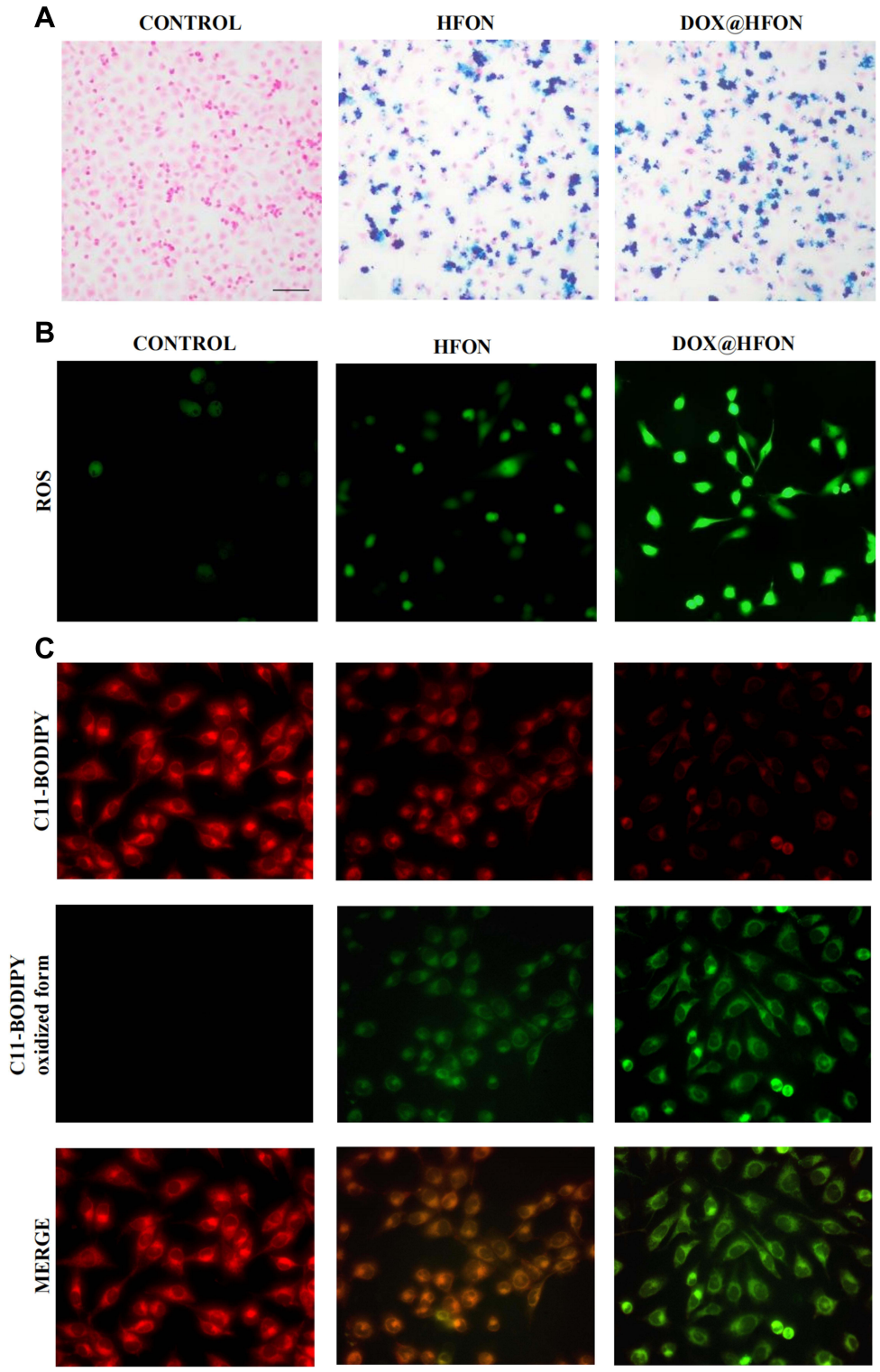

Figure 4 (**A**) Prussian blue staining image of cells treated with HFON and DOX@HFON; (**B**) ROS generate levels of MDA-MB-231 cells in vitro; (**C**) Fluorescence images of DOX@HFON treated cells after staining by C11-BODIPY.

of the targeted group and the HFON group were statistically different. This also confirms the hypothesis that DOX in DOX@HFON can efficiently generate •OH and catalyze the generation of a large amount of ROS through the Fenton reaction.

Lipid peroxidation can cause serious damage to cell membrane, lipoprotein and other lipid-containing structures, including damage to DNA and proteins, and then affect the normal function of cells. The process of LPO is the process of oxidation of cell membrane by ROS, which leads to the change of cell structure and function. C11-BODIPY, as a fluorescent probe with both oxidation sensitivity and LPO specificity, is compatible with cell membrane structure. Combined with the production of ROS, we evaluated LPO. During the oxidation reaction, the fluorescence group on the C11-BODIPY probe will change from red to green, and there is strong red fluorescence in the cells in Figure 4C control group, which is the state of redox dynamic equilibrium, and the gradually enhanced green fluorescence signal and weakening red fluorescence signal can be seen in HFON group, indicating the occurrence of oxidation reaction. The strong green fluorescence signal in the final group indicated that DOX@HFON could induce lipid peroxidation and lead to changes in the structure and function of tumor cells. This is consistent with the production level of ROS, the accumulation of intracellular iron ions and the joint effect of ROS, which further confirms that DOX@HFON induces autophagy and apoptosis of tumor cells through the mechanism of ferroptosis.

In vitro Cytotoxic Effects

In this experiment, the killing effect of DOX@HFON on MDA-MB-231 cells (Figure S3) was determined by CCK-8. It can be seen that DOX@HFON group can inhibit the activity of MDA-MB-231 cells in varying degrees, and the activity of MDA-MB-231 cells decreases gradually with the increase of drug concentration, which reflects the feasibility of chemotherapy combined with Fenton reaction in tumor treatment.

Then, we detected the apoptosis level of MDA-MB-231 cells. It can be seen from the results (Figures 5A and S4) that the apoptosis level of the cells in the HFON group has a tendency to increase compared with the control group (**P<0.01), which confirms that HFON has a certain pro-apoptotic effect on tumor cells. DOX@HFON Compared

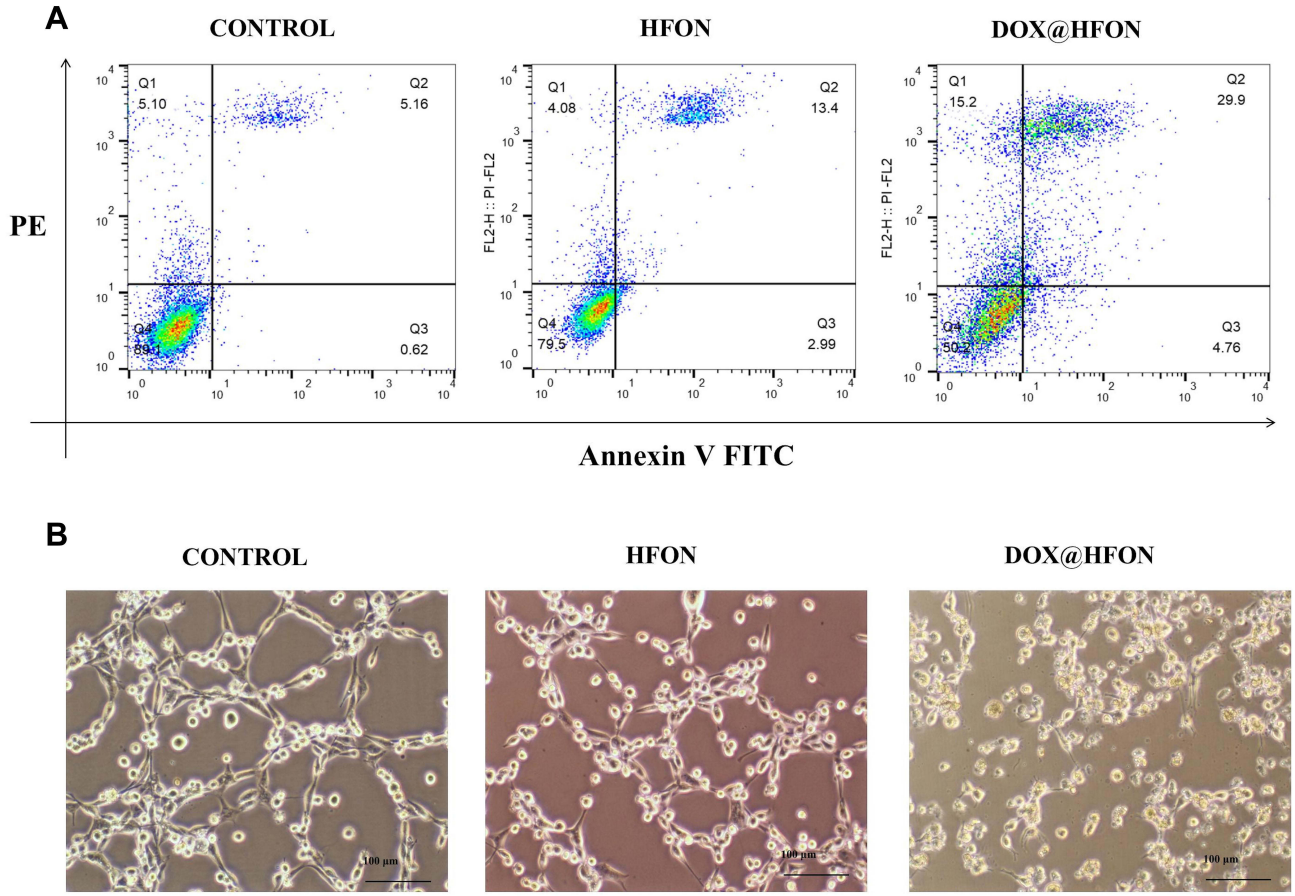

Figure 5 (**A**) poptosis levels of the cells in different groups. (**B**) The levels of angiogenesis in different treatment groups.

with the Control group and HFON group, the apoptosis level of the cells in the group was significantly increased, which means that the Fenton reaction effectively promoted the tumor cells to produce ROS-induced apoptosis with a killing effect.

As we all know, blood vessels are the lifeblood of the growth and development of malignant tumors. If the angiogenesis in the tumor tissue can be inhibited, it will cut off the tumor nutrition supply and achieve the effect of tumor starvation treatment. Therefore, we explored the effects of HFON and DOX@HFON on angiogenesis. HUVEC, whose full name is Human Umbilical Vein Endothelial Cells, is usually selected as a cell model in vascular endothelial experiments. In this experiment, HUVEC cells were selected as the research object of the effect of drugs on angiogenesis, that is, the toxic effects of HFON and DOX@HFON on HUVEC cells. From Figures 5B and S5, we unexpectedly found that both HFON and DOX@HFON had a certain inhibitory effect on proliferation of HUVEC cells (***P<0.001), and the inhibitory effect of DOX@HFON group was very significant. Compared with the Control group, the DOX@HFON group reduced about 90% of angiogenesis by inhibiting the proliferation of HUVEC cells, thus reducing the level of angiogenesis.

Therapeutic Effect in vivo

From cell experiments, we found that DOX@HFON mediates the killing effect of Fenton reaction on MDA-MB-231 cells. In order to further test the effect of DOX@HFON in vivo, we treated tumor-bearing mice and observed tumor cells. Growth and weight changes of mice. Figure 6A shows the model of tumor-bearing mice combined with exogenous magnetic field targeted therapy. After 18 days of treatment, it could be observed that the mean tumor volume of the MAGMET@DOX@HFON group was significantly smaller than that of the other three groups (Figures S6 and S7) (***P<0.001). In the process of monitoring the tumor volume and weight of mice, it was found that compared with the Control group, the HFON group, DOX@HFON group and MAGMET@DOX@HFON group had different degrees of inhibition on tumor growth on the 6th day of treatment. With the progress of the treatment, the tumors in the HFON group showed a slow growth trend, which was due to the EPR effect. When HFON reached the tumor site, it could react with H_2O_2 to generate ROS to inhibit tumor growth. Compared with the HFON group, DOX@HFON and MAGMET@DOX@HFON significantly inhibited tumor growth, and the treatment effect of the MAGMET@DOX@HFON group was particularly significant (Figure 6B–D), because the exogenous magnetic field could efficiently aggregate DOX@HFON in vivo to the tumor. In the tissue, while releasing DOX to kill the tumor by chemotherapy, HFON provides a large amount of iron ions, which induces the generation of ROS and causes tumor cell apoptosis and necrosis. During the treatment period, there was no obvious abnormality in the body weight of the mice (Figure 6E). The results of in vivo treatment experiments showed that: HFON, DOX@HFON and MAGMET@DOX@HFON can inhibit tumors, the inhibition ability is sequentially enhanced, and has great biological safety.

In vivo Biodistribution of Nanoparticles

In order to explore the DOX@HFON MRI imaging effect in vivo, this experiment used GE 3.0T MRI to conduct imaging research on mice. As can be seen from Figures 7A and S8, compared with the T2 signal intensity of tumor tissue at 0 h, the tumor tissue of DOX@HFON group and MAGNET@DOX@HFON group has a darkening trend with time, and the MAGNET@DOX@HFON group has a significant trend of darkening over time. This result confirms the great MRI imaging effect of DOX@HFON in mice tumors, and the feasibility of the nano-diagnosis and treatment platform with additional exogenous magnetic field for targeted tumor therapy.

In vitro experiments found that there was a large amount of Fe enrichment in MDA-MB-231 cells treated with HFON and DOX@HFON. Therefore, the enrichment of iron ion in tumor tissue was further detected in animal experiments. As shown in Figure 7B, it can be found that no Fe were detected in the tumor tissue of the Control group, while a small amount of blue staining was found in the tumor tissue of the DOX@HFON group. It is worth noting that a large amount of blue staining was detected in the tumor tissue sections of the MAGNET@DOX@HFON group, which further confirmed the effectiveness of the nano-diagnosis and treatment platform, and provided a solid and powerful basis for the occurrence of Fenton reaction.

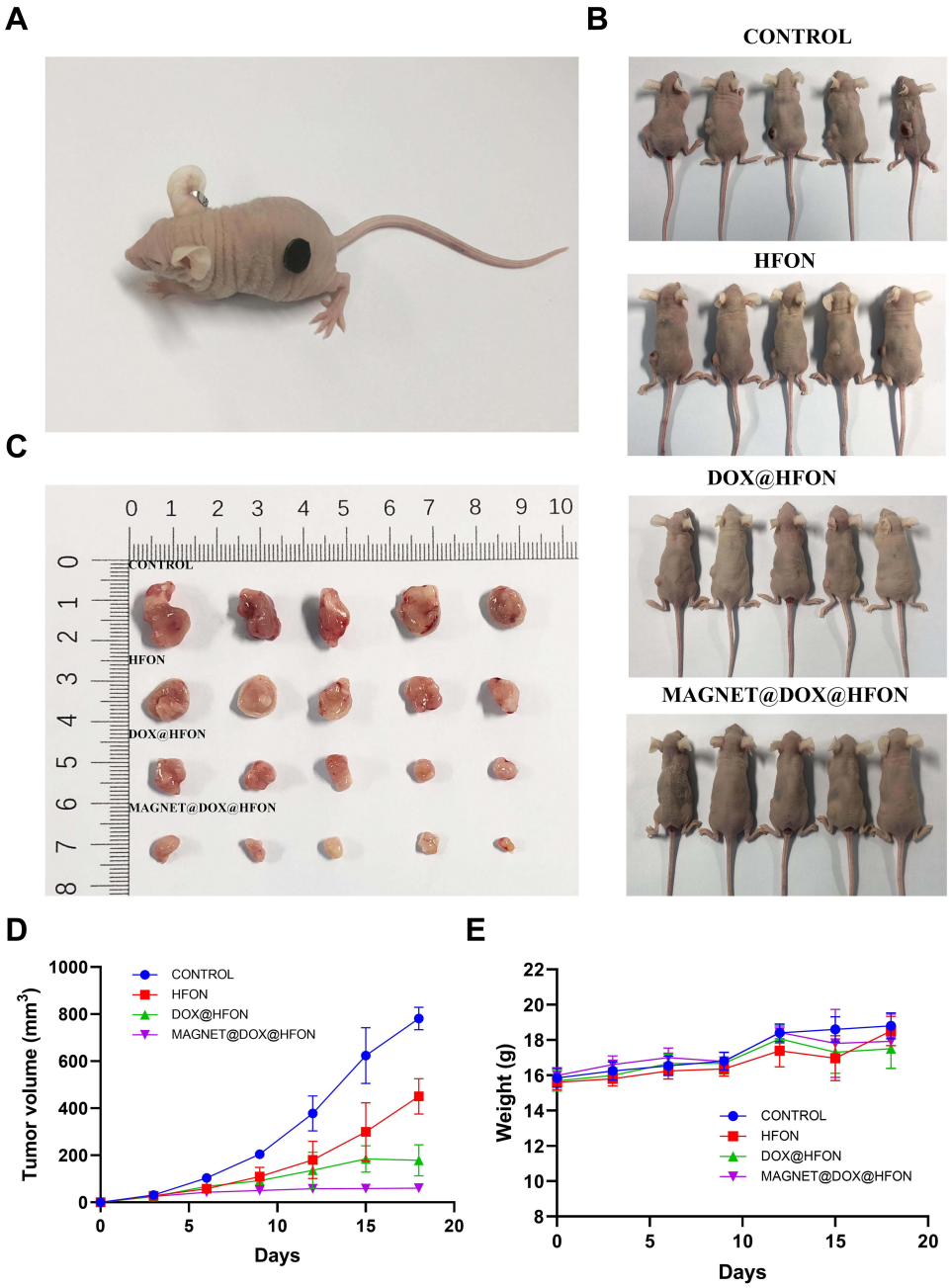

Figure 6 Evaluation of treatment effect in tumor-bearing mice in vivo: (**A**) Magnetic targeting model of tumor-bearing mice; (**B**) Pictures of the mice at the end of treatment; (**C**) Anatomical image of tumors in different groups of mice after 21 days of treatment; (**D**) Tumor volume curve of tumors during treatment; (**E**) Treatment process changes in body weight of mice.

Histological Significance of Tumors

To understand the tumor-killing mechanism of MAGNET@DOX@HFON, we performed H&E staining, CD31, Ki-67, ROS, LPO immunofluorescence and TUNEL apoptosis detection on mice tumor sections (Figures 8 and S9). The changes of cell integrity and tissue morphology were observed by H&E staining. The edge of tumor tissue in the Control group was clear and no obvious necrosis was found, while in the MAGNET@DOX@HFON group after targeted therapy, the apoptotic and necrotic areas in the tumor tissue were significantly increased; CD31 represents the level of tumor angiogenesis, and the expression level in the MAGNET@DOX@HFON group is significantly lower than the other three groups, reflecting that MAGNET@DOX@HFON also has a very significant effect in inhibiting angiogenesis; proliferation can be observed in the Control group; the high expression level of the marker Ki-67, while there is little red

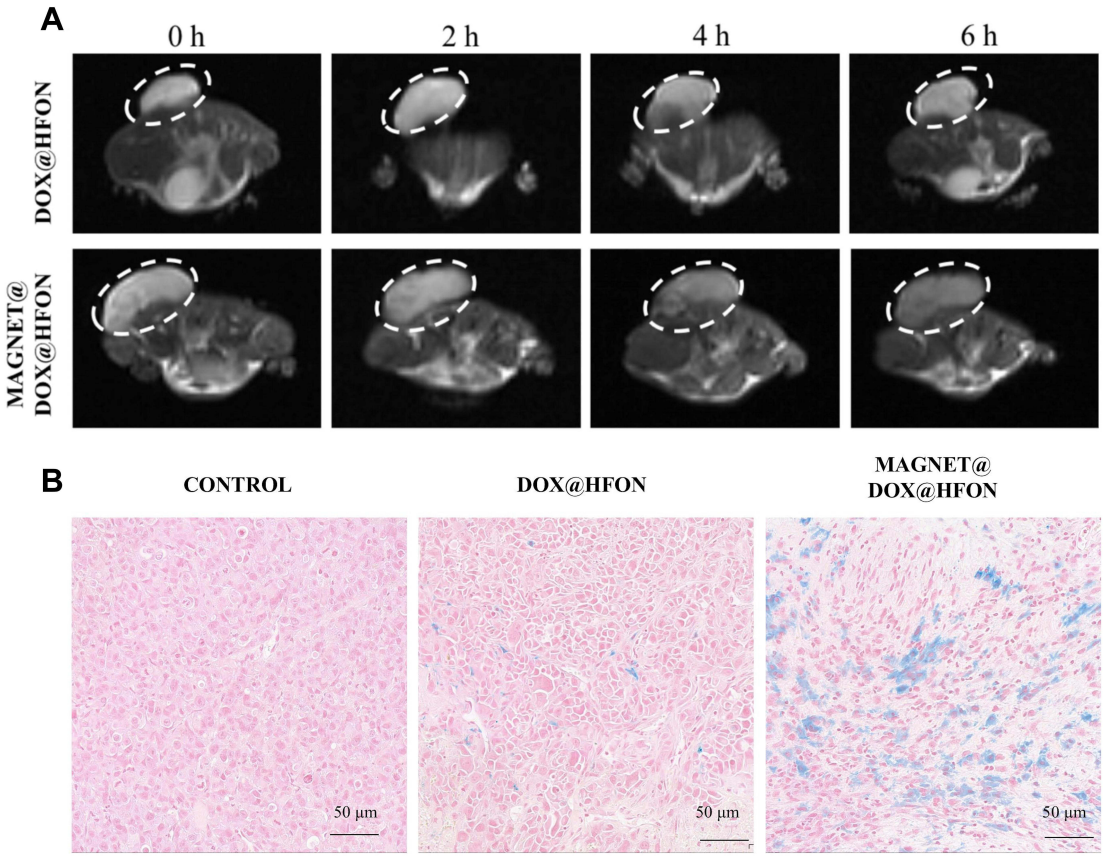

Figure 7 (**A**) MRI T2-weighted imaging of mice in DOX@HFON and MAGNET@DOX@HFON groups before and after drug injection; (**B**) Prussian blue staining of transplanted tumor sections of mice in different groups.

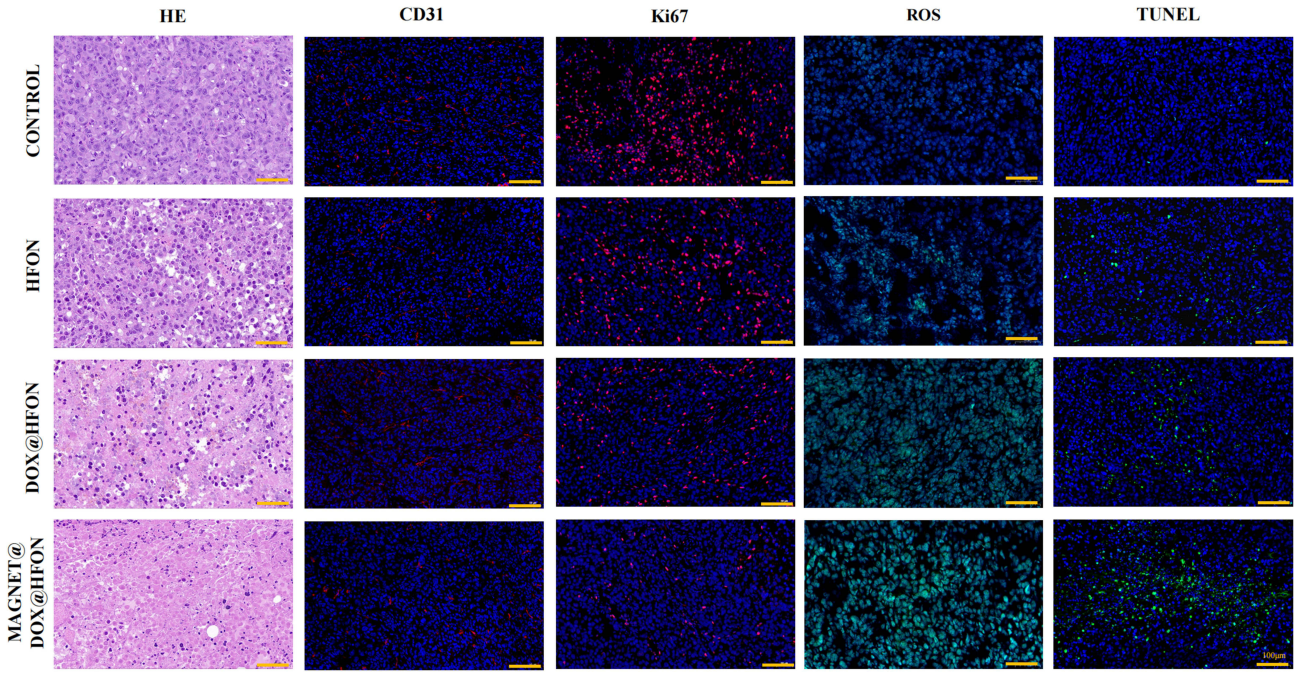

Figure 8 H&E, CD31, Ki-67, ROS immunofluorescence staining and TUNEL apoptosis detection pictures of tumor sections in each group (the scale bar is 100μm).

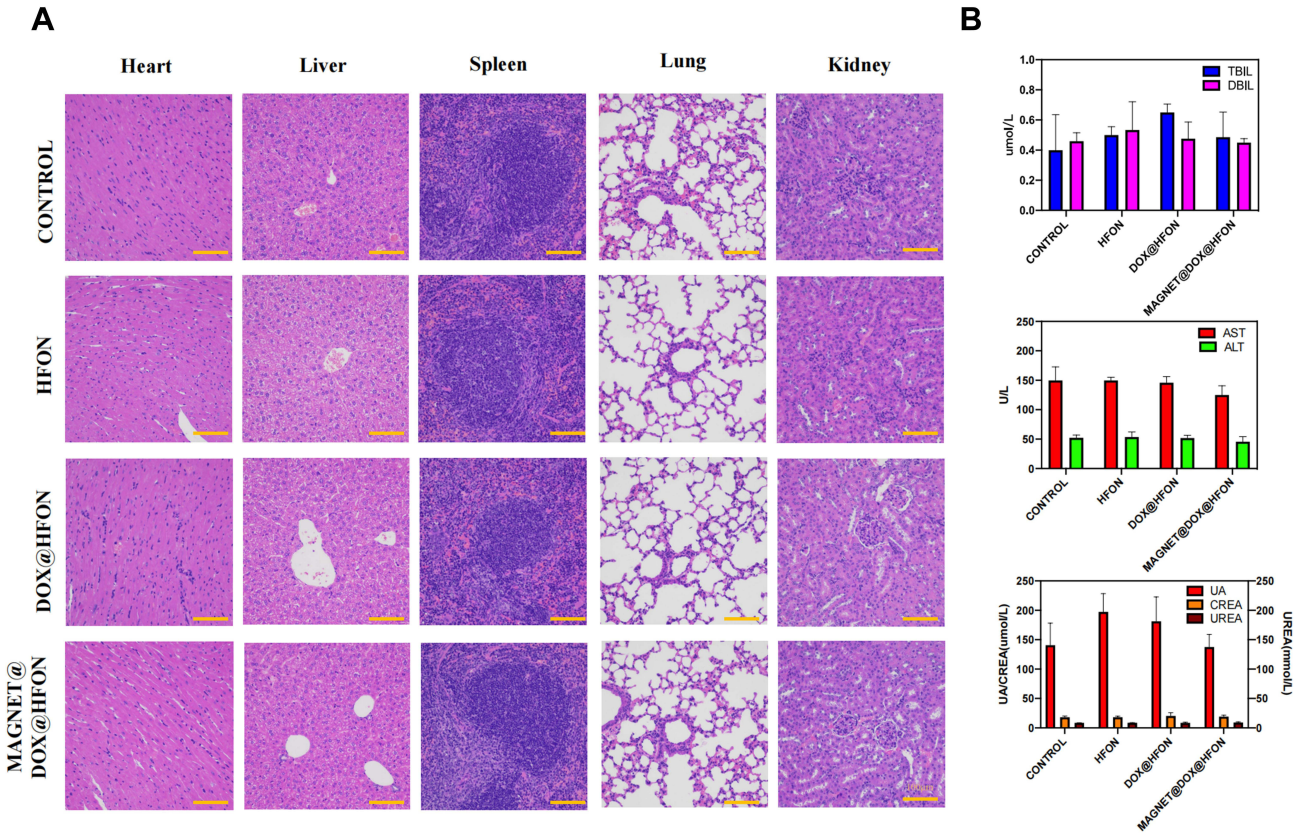

Figure 9 (**A**) H&E staining of the main organs of mice; (**B**) Blood biochemical examination of tumor-bearing mice after different treatments.

fluorescence signal in MAGNET@DOX@HFON, indicates that MAGNET@DOX@HFON can effectively inhibit the proliferation of cancer cells; ROS staining showed that the expression of ROS in the tissue increased gradually, and the green fluorescence signal was the strongest in the MAGNET@DOX@HFON group; LPO fluorescence staining showed a wide range of green fluorescence staining in the tumor tissue treated with MAGNET@DOX@HFON, which confirmed that high concentration of Fe enriched in the tumor tissue and produced a large amount of ROS, which further enhanced lipid peroxidation and induced ferroptosis; TUNEL staining was used to evaluate the apoptosis of tumor cells. In the final group, a large number of green fluorescence signals confirmed the ability of MAGNET@DOX@HFON to efficiently promote apoptosis. It can be seen that DOX@HFON has a strong killing effect on tumor tissue, and the therapeutic effect is more significant after adding an exogenous magnetic field to guide targeting, which once again verifies the effectiveness of the combination of chemotherapy drugs based on Fenton reaction on tumor treatment.

Biosafety Experiment

As can be seen from Figure 9A and B, no obvious abnormal pathological changes were found in the heart, liver, spleen, lung and kidney tissues of the mice in the Control group, HFON group, DOX@HFON group and MAGMET@DOX@HFON group. In addition, the detection of blood biochemical indexes in mice showed that there was no significant difference between the results of each experimental group and the control group ($P >$ ns). It is further confirmed that the nanomaterials prepared in this experiment has great biological safety.

Discussion

In recent years, various drug-loaded nanoparticles have been widely used in tumor therapy.[33–36] Compared with magnetic targeting of tumor-specific ligands, the magnetically guided nanotherapeutic platform is not limited to the type of tumor surface receptors, making it potentially useful in the treatment of solid tumors. In addition, a large number of studies have

shown that Fe_3O_4 has the potential to be used as a contrast agent for MRI T2-weighted imaging, which can be used for imaging evaluation of tumor sites by adjusting the relaxation rate, so as to achieve the purpose of tumor screening and diagnosis.[37–39] With reference to many nanomaterials, we have prepared HFON with high drug loading/release rate, great stability in vitro, superparamagnetic and biological safety as an effective carrier for this experiment, which has laid a great foundation for the tumor treatment.

HFON can also mediate the occurrence of Fenton reaction for tumor therapy.[40,41] Liang et al reported a new strategy to stabilize Fe via Fe/Fe_3O_4 (PYSNPs) under normal physiological conditions and promote the occurrence of Fenton reaction by controlling the release of Fe in the TME to improve the efficacy of tumor therapy.[42] Similar to the study of Liang et al, a large amount of Fe accumulation was observed in the cells and tumor tissues of the DOX@HFON group in this experiment. It is converted to highly toxic •OH through the Fenton reaction, resulting in irreversible oxidative damage to lipids, proteins and DNA.[43] At the same time, hypoxia and acidity are notable characteristics of TME. Weak acidity TME can effectively promote the rapid separation of Fe^{2+} and Fe^{3+} from HFON, which further induces the occurrence of Fenton reaction. It is worth noting that in this experiment, in addition to the occurrence of the acidic environment stimulation reaction in the TME, the loaded chemotherapeutic drug DOX can also generate H_2O_2 during tumor treatment, it was also confirmed by ESR detection that there was an additional cytotoxic OH in DOX@HFON, providing a steady stream of raw materials for the occurrence of the Fenton reaction,[42,44] play a certain synergistic therapeutic effect.

Studies have shown that excessive production of ROS can disrupt redox homeostasis, limit the functional structure of mitochondria, and lead to cell apoptosis.[45] Both DOX and ROS have been reported to induce autophagy and death of tumor cells.[46,47] Morphologically, Scott J and Feng et al found that mitochondrial volume was significantly reduced after autophagy, mitochondrial cristae decreased and membrane density increased,[48,49] and an increase in autophagic lysosomes was also reported that related to excess ROS,[50–52] and these views have been verified in this experiment, with certain reliability and authenticity. In addition, through the results of TEM, we also found that MDA-MB-231 cells had changes in cell membrane morphology, nuclear pyknosis, and cytoplasmic vacuolization, which was mainly attributed to DOX@HFON ability to effectively induce autophagy in tumor cells apoptosis. At the same time, the production of a large number of ROS breaks the original redox dynamic balance in the body, which further induces the occurrence and development of LPO, resulting in serious damage to protein and DNA, as well as changes in cell structure, and accelerates apoptosis, autophagy and ferroptosis of tumor cells.

Targeted therapy, also known as “biological missile”, can specifically select carcinogenic sites in the body for binding, and then play a role in therapy, causing specific death of tumor cells without affecting the normal tissues around the tumor. Wang et al constructed a Fe_3O_4@C@MIL-100(Fe) nanocomposite, which was guided by an exogenous magnetic field to target the tumor site for the purpose of targeted therapy.[30] In this way, the efficient killing effect of MAGNET@DOX@HFON on tumors is due to the fact that DOX is targeted and delivered to tumor cells, causing damage to tumor cell DNA and generating ROS, and at the same time increasing the concentration of H_2O_2 in TME, promoting the on the other hand, it is attributed to HFON “amplifying” the reaction between Fe and H_2O_2 in cells, thereby further increasing the production of ROS in the environment of exogenous magnetic field. Interestingly, during the research process, we also discovered the great potential of DOX@HFON in inhibiting angiogenesis, which can effectively cut off the nutrient supply of tumors to achieve the purpose of starvation treatment, which is also the targeted therapy for TNBC by the nano-diagnosis and treatment platform provides a new idea.

Conclusion

We have successfully constructed a novel nano-diagnosis and treatment platform, using the hollow and porous characteristics of HFON to successfully load DOX. The nanoparticles are effectively delivered to the tumor site by magnetic targeting to achieve specific infusion in the tumor tissue, induce autophagy, apoptosis and of tumor cells in the environment of high concentration of Fe, kill tumor tissue, cooperate with Fenton reaction, and rely on the great MRI imaging effect of HFON, so that this study has a certain clinical application value and development prospect in the field of tumor therapy. It also brings hope for the treatment of TNBC!

Data Sharing Statement

The raw data supporting the conclusions of this article will be made available by the authors, without undue reservation.

Ethics Statement

The animal study was reviewed and approved by Affiliated Tumor Hospital of Guangxi Medical University.

Acknowledgments

We would like to thank the Guangxi Key Laboratory of Early Prevention and Treatment for Regional High Frequency Tumors (Affiliated Tumor hospital, Guangxi Medical University) for providing facilities and support throughout our research.

Author Contributions

All authors made a significant contribution to the work reported, whether that is in the conception, study design, execution, acquisition of data, analysis and interpretation, or in all these areas; took part in drafting, revising or critically reviewing the article; gave final approval of the version to be published; have agreed on the journal to which the article has been submitted; and agree to be accountable for all aspects of the work.

Funding

This work was supported by the National Natural Science Foundation of China (82160341) and Guangxi Key Research and Development Program (2022GXNSFDA035060).

Disclosure

The authors report no conflicts of interest in this work.

References

1. Ferrari M. Cancer nanotechnology: opportunities and challenges. *Nat Rev Cancer*. 2005;5(3):161–171. doi:10.1038/nrc1566
2. Anders CK, Carey LA. Biology, metastatic patterns, and treatment of patients with triple-negative breast cancer. *Clin Breast Cancer*. 2009;9(Suppl 2):S73–S81. doi:10.3816/CBC.2009.s.008
3. Gupta GK, Collier AL, Lee D, et al. Perspectives on triple-negative breast cancer: current treatment strategies, unmet needs, and potential targets for future therapies. *Cancers*. 2020;12:9. doi:10.3390/cancers12092392
4. Wang H, Agarwal P, Zhao S, et al. Hyaluronic acid-decorated dual responsive nanoparticles of Pluronic F127, PLGA, and chitosan for targeted co-delivery of doxorubicin and irinotecan to eliminate cancer stem-like cells. *Biomaterials*. 2015;72:74–89. doi:10.1016/j.biomaterials.2015.08.048
5. Thorn CF, Oshiro C, Marsh S, et al. Doxorubicin pathways: pharmacodynamics and adverse effects. *Pharmacogenet Genomics*. 2011;21 (7):440–446. doi:10.1097/FPC.0b013e32833ffb56
6. Harris L, Batist G, Belt R, et al. Liposome-encapsulated doxorubicin compared with conventional doxorubicin in a randomized multicenter trial as first-line therapy of metastatic breast carcinoma. *Cancer*. 2002;94(1):25–36. doi:10.1002/cncr.10201
7. Zheng X, Zhao Y, Jia Y, et al. Biomimetic co-assembled nanodrug of doxorubicin and berberine suppresses chemotherapy-exacerbated breast cancer metastasis. *Biomaterials*. 2021;271:120716. doi:10.1016/j.biomaterials.2021.120716
8. Sha Z, Yang S, Fu L, et al. Manganese-doped gold core mesoporous silica particles as a nanoplatform for dual-modality imaging and chemo-chemodynamic combination osteosarcoma therapy. *Nanoscale*. 2021;13(9):5077–5093. doi:10.1039/D0NR09220G
9. Xu J, Pan X, Hu Z. MiR-502 mediates esophageal cancer cell TE1 proliferation by promoting AKT phosphorylation. *Biochem Biophys Res Commun*. 2018;501(1):119–123. doi:10.1016/j.bbrc.2018.04.188
10. Arumov A, Liyanage PY, Trabolsi A, et al. Optimized doxorubicin chemotherapy for diffuse large b-cell lymphoma exploits nanocarrier delivery to transferrin receptors. *Cancer Res*. 2021;81(3):763–775. doi:10.1158/0008-5472.CAN-20-2674
11. Xiong H, Wang C, Wang Z, Jiang Z, Zhou J, Yao J. Intracellular cascade activated nanosystem for improving ER+ breast cancer therapy through attacking GSH-mediated metabolic vulnerability. *J Control Release*. 2019;309:145–157. doi:10.1016/j.jconrel.2019.07.029
12. Gao J, Xiong Y, Ho Y-S, et al. Glutathione peroxidase 1-deficient mice are more susceptible to doxorubicin-induced cardiotoxicity. *Biochim Biophys Acta*. 2008;1783(10):2020–2029. doi:10.1016/j.bbamcr.2008.05.027
13. Carvalho C, Santos RX, Cardoso S, et al. Doxorubicin: the good, the bad and the ugly effect. *Curr Med Chem*. 2009;16(25):3267–3285. doi:10.2174/092986709788803312
14. Zhu L, Lin M. The synthesis of nano-doxorubicin and its anticancer effect. *Anticancer Agents Med Chem*. 2021;21(18):2466–2477. doi:10.2174/1871520621666201229115612
15. Waterhouse DN, Tardi PG, Mayer LD, Bally MB. A comparison of liposomal formulations of doxorubicin with drug administered in free form: changing toxicity profiles. *Drug Saf*. 2001;24(12):903–920. doi:10.2165/00002018-200124120-00004
16. Shafei A, El-Bakly W, Sobhy A, et al. A review on the efficacy and toxicity of different doxorubicin nanoparticles for targeted therapy in metastatic breast cancer. *Biomed Pharmacother*. 2017;95:1209–1218. doi:10.1016/j.biopha.2017.09.059

17. Barenholz Y. Doxil(R)–the first FDA-approved nano-drug: lessons learned. *J Control Release*. 2012;160(2):117–134. doi:10.1016/j.jconrel.2012.03.020
18. Gabizon A, Shmeeda H, Barenholz Y. Pharmacokinetics of pegylated liposomal Doxorubicin: review of animal and human studies. *Clin Pharmacokinet*. 2003;42(5):419–436. doi:10.2165/00003088-200342050-00002
19. Rivankar S. An overview of doxorubicin formulations in cancer therapy. *J Cancer Res Ther*. 2014;10(4):853–858. doi:10.4103/0973-1482.139267
20. Alavi M, Hamidi M. Passive and active targeting in cancer therapy by liposomes and lipid nanoparticles. *Drug Metab Pers Ther*. 2019;34:1.
21. Qian X, Zhang J, Gu Z, Chen Y. Nanocatalysts-augmented Fenton chemical reaction for nanocatalytic tumor therapy. *Biomaterials*. 2019;211:1–13. doi:10.1016/j.biomaterials.2019.04.023
22. Wang D, Feng C, Xiao Z, et al. Therapeutic hydrogel for enhanced immunotherapy: a powerful combination of MnO2 nanosheets and vascular disruption. *Nano Today*. 2022;47:1. doi:10.1016/j.nantod.2022.101673
23. Gorrini C, Harris IS, Mak TW. Modulation of oxidative stress as an anticancer strategy. *Nat Rev Drug Discov*. 2013;12(12):931–947. doi:10.1038/nrd4002
24. He J, Yang X, Men B, Wang D. Interfacial mechanisms of heterogeneous Fenton reactions catalyzed by iron-based materials: a review. *J Environ Sci*. 2016;39:97–109. doi:10.1016/j.jes.2015.12.003
25. Kwon B, Han E, Yang W, et al. Nano-Fenton reactors as a new class of oxidative stress amplifying anticancer therapeutic agents. *ACS Appl Mater Interfaces*. 2016;8(9):5887–5897. doi:10.1021/acsami.5b12523
26. Wang D, Zhou J, Fang W, et al. A multifunctional nanotheranostic agent potentiates erlotinib to EGFR wild-type non-small cell lung cancer. *Bioact Mater*. 2022;13:312–323. doi:10.1016/j.bioactmat.2021.10.046
27. Sui C, Tan R, Chen Y, et al. MOFs-derived Fe–N codoped carbon nanoparticles as O2-evolving reactor and ROS generator for CDT/PDT/PTT synergistic treatment of tumors. *Bioconjug Chem*. 2021;32(2):318–327. doi:10.1021/acs.bioconjchem.0c00694
28. Kumar B, Koul S, Khandrika L, Meacham RB, Koul HK. Oxidative stress is inherent in prostate cancer cells and is required for aggressive phenotype. *Cancer Res*. 2008;68(6):1777–1785. doi:10.1158/0008-5472.CAN-07-5259
29. Xu X, Chen Y, Zhang Y, Yao Y, Ji P. Highly stable and biocompatible hyaluronic acid-rehabilitated nanoscale MOF-Fe 2+ induced ferroptosis in breast cancer cells. *J Mater Chem B*. 2020;8(39):9129–9138. doi:10.1039/D0TB01616K
30. Wang D, Zhou J, Chen R, et al. Magnetically guided delivery of DHA and Fe ions for enhanced cancer therapy based on pH-responsive degradation of DHA-loaded Fe3O4@C@MIL-100(Fe) nanoparticles. *Biomaterials*. 2016;107:88–101. doi:10.1016/j.biomaterials.2016.08.039
31. Wang D, Nie T, Huang C, et al. Metal-cyclic dinucleotide nanomodulator-stimulated STING signaling for strengthened radioimmunotherapy of large tumor. *Small*. 2022;18(41):e2203227. doi:10.1002/smll.202203227
32. Qiu G, Xue L, Zhu X, et al. Cetuximab combined with sonodynamic therapy achieves dual-modal image monitoring for the treatment of EGFR-sensitive non-small-cell lung cancer. *Front Oncol*. 2022;12:1.
33. Nam KC, Han YS, Lee JM, Kim SC, Cho G, Park BJ. Photo-functionalized magnetic nanoparticles as a nanocarrier of photodynamic anticancer agent for biomedical theragnostics. *Cancers*. 2020;12(3):571. doi:10.3390/cancers12030571
34. Liu GX, Fang GQ, Xu W. Dual targeting biomimetic liposomes for paclitaxel/DNA combination cancer treatment. *Int J Mol Sci*. 2014;15(9):15287–15303. doi:10.3390/ijms150915287
35. Lv R, Jiang X, Yang F, et al. Degradable magnetic-response photoacoustic/up-conversion luminescence imaging-guided photodynamic/photothermal antitumor therapy. *Biomater Sci*. 2019;7(11):4558–4567. doi:10.1039/C9BM00853E
36. Hou H, Huang X, Wei G, Xu F, Wang Y, Zhou S. Fenton reaction-assisted photodynamic therapy for cancer with multifunctional magnetic nanoparticles. *ACS Appl Mater Interfaces*. 2019;11(33):29579–29592. doi:10.1021/acsami.9b09671
37. Al Faraj A, Shaik AS, Halwani R, Alfuraih A. Magnetic targeting and delivery of drug-loaded SWCNTs theranostic nanoprobes to lung metastasis in breast cancer animal model: noninvasive monitoring using magnetic resonance imaging. *Mol Imaging Biol*. 2016;18(3):315–324. doi:10.1007/s11307-015-0902-0
38. Grootendorst DJ, Jose J, Fratila RM, et al. Evaluation of superparamagnetic iron oxide nanoparticles (Endorem(R)) as a photoacoustic contrast agent for intra-operative nodal staging. *Contrast Media Mol Imaging*. 2013;8(1):83–91. doi:10.1002/cmmi.1498
39. Gao Z, Ma T, Zhao E, et al. Small is smarter: nano mri contrast agents - advantages and recent achievements. *Small*. 2016;12(5):556–576. doi:10.1002/smll.201502309
40. Zhou Z, Song J, Tian R, et al. Activatable singlet oxygen generation from lipid hydroperoxide nanoparticles for cancer therapy. *Angew Chem Int Ed Engl*. 2017;56(23):6492–6496. doi:10.1002/anie.201701181
41. Khan MI, Mohammad A, Patil G, Naqvi SA, Chauhan LK, Ahmad I. Induction of ROS, mitochondrial damage and autophagy in lung epithelial cancer cells by iron oxide nanoparticles. *Biomaterials*. 2012;33(5):1477–1488. doi:10.1016/j.biomaterials.2011.10.080
42. Ghazanfari MR, Kashefi M, Shams SF, Jaafari MR. Perspective of Fe3O4 nanoparticles role in biomedical applications. *Biochem Res Int*. 2016;2016:7840161. doi:10.1155/2016/7840161
43. Ke W, Li J, Mohammed F, et al. Therapeutic polymersome nanoreactors with tumor-specific activable cascade reactions for cooperative cancer therapy. *ACS Nano*. 2019;13(2):2357–2369. doi:10.1021/acsnano.8b09082
44. Qi C, Wang W, Wang P, et al. Facile synthesis of Fe3o4@Au/PPy-DOX nanoplatform with enhanced glutathione depletion and controllable drug delivery for enhanced cancer therapeutic efficacy. *Molecules*. 2022;27:13. doi:10.3390/molecules27134003
45. Lin LS, Song J, Song L, et al. Simultaneous Fenton-like ion delivery and glutathione depletion by MnO2 -based nanoagent to enhance chemodynamic therapy. *Angew Chem Int Ed Engl*. 2018;57(18):4902–4906. doi:10.1002/anie.201712027
46. Li Y, Zeng X, Lu D, Yin M, Shan M, Gao Y. Erastin induces ferroptosis via ferroportin-mediated iron accumulation in endometriosis. *Hum Reprod*. 2021;36(4):951–964. doi:10.1093/humrep/deaa363
47. Wang X, Li X, Liang X, et al. ROS-responsive capsules engineered from green tea polyphenol-metal networks for anticancer drug delivery. *J Mater Chem B*. 2018;6(7):1000–1010. doi:10.1039/C7TB02688A
48. Chen X, Li J, Kang R, Klionsky DJ, Tang D. Ferroptosis: machinery and regulation. *Autophagy*. 2021;17(9):2054–2081. doi:10.1080/15548627.2020.1810918
49. Feng H, Stockwell BR. Unsolved mysteries: how does lipid peroxidation cause ferroptosis? *PLoS Biol*. 2018;16:5. doi:10.1371/journal.pbio.2006203

50. Tappia P, Dent M, Dhalla N. Oxidative stress and redox regulation of phospholipase D in myocardial disease☆. *Free Radic Biol Med*. 2006;41 (3):349–361. doi:10.1016/j.freeradbiomed.2006.03.025
51. Filomeni G, De Zio D, Cecconi F. Oxidative stress and autophagy: the clash between damage and metabolic needs. *Cell Death Differ*. 2015;22 (3):377–388. doi:10.1038/cdd.2014.150
52. Wang D, Zhang M, Zhang Y, et al. Intraparticle double-scattering-decoded sonogenetics for augmenting immune checkpoint blockade and CAR-T therapy. *Adv Sci*. 2022;93:2203106.